3D Metal-Only Phoenix Cell and its Application for Transmit-reflect-array

Zhihang An, Tony Makdissy, M. García-Vigueras, Sébastien Vaudreuil, Raphael Gillard

To cite this version:

Zhihang An, Tony Makdissy, M. García-Vigueras, Sébastien Vaudreuil, Raphael Gillard. 3D Metal-Only Phoenix Cell and its Application for Transmit-reflect-array. IEEE Access, 2023, Ieee Access, 11, pp.137343-137351. 10.1109/access.2023.3338150 . hal-04356744

HAL Id: hal-04356744
https://hal.science/hal-04356744v1

Submitted on 20 Dec 2023

IEEE Access
Multidisciplinary ⁝ Rapid Review ⁝ Open Access Journal

Date of publication xxxx 00, 0000, date of current version xxxx 00, 0000.

Digital Object Identifier 10.1109/ACCESS.2017.Doi Number

3D Metal-Only Phoenix Cell and its Application for Transmit-reflect-array

Zhihang An[1], Tony Makdissy[2], María García-Vigueras[1], Sébastien Vaudreuil[3], Raphaël Gillard[1]
[1]UMR CNRS 6164, INSA Rennes, IETR, 35708 Rennes, France.
[2]TICKET Research Laboratory, Antonine University, 40016 Hadat-Baadba, Lebanon
[3]Euromed University of Fes, 51 30 030 Fès, Morocco

Corresponding author: Zhihang AN (e-mail: zhihang.an@outlook.com).

The work was jointly funded by the Agence Universitaire de la Francophonie (Moyen-Orient) and the National Council for Scientific Research Lebanon (CNRS-L). This work was also supported by the European Union, the French Ministery of Higher Education and Research, Brittany Region and Rennes Metropole through CPER funding.

ABSTRACT This paper presents a 3D metal-only waveguide-based phoenix cell. The proposed cell uses open-ended waveguides, which allow a portion of the incident wave to pass through the phoenix cell. It thus has the ability to control both reflection and transmission phases. Its principle is analyzed in detail. Two metal-only transmit-reflect-array antennas are then designed. The proposed transmit-reflect-array antennas are able to produce both transmitted and reflected beams at 16GHz in the target directions simultaneously. One of the transmit-reflect-array antennas is fabricated using selective laser melting 3D printing technology. The measured results show that a good agreement between the simulated and measured radiation patterns is achieved. The side lobe and cross polarization levels at 16 GHz are -15.3 dB and -23.1 dB respectively. The measured gain of transmitted and reflected beams at 16GHz are 25.7 dBi and 24.1 dBi respectively. Both the simulation and measurement results fully demonstrate the capabilities of the proposed 3D metal-only phoenix cell.

INDEX TERMS metal-only, phoenix cell, transmit-reflect-array, waveguide

I. INTRODUCTION

Reflectarray antennas (RAs) can be seen as a combination of antenna arrays and reflector antennas with the advantages of high gain, low profile, low cost and easy manufacturing. They are usually implemented in microstrip technology, by printing metallic resonators on top of a dielectric substrate backed by a ground plane. Among other possible solutions, the Phoenix Cell (PC) is a topology of RA cell with high potential [1-8]. In its original version [1], it consists of two square concentric rings enclosing a square patch. The geometrical variation over the RA aperture is smoothed owing to the rebirth ability of the PC. In the literature, PCs are typically implemented using dielectric materials, which makes them not optimal for some applications operating in severe environments, such as space. In such situations, metal-only reflectarrays (MORA) are preferable, as they avoid the intrinsic problems brought by the dielectric materials such as outgassing, losses, and temperature-dependent dielectric constant [9].

Transmitarray antennas (TA) emerge in this context as the solution allowing to overcome certain limitations associated to RA, such as feed-blockage [10]. Indeed, a RA produces a reflected beam while a TA generates a transmitted one. The combination of both RA and TA functionalities in a single-feed high-gain transmit-reflect-array (TRA) has been found of great interest in order to implement bi-directional radiated beams. For example, [11] proposes a TRA based on a multilayer amplitude–phase-modulated stack-up and employing sparse-array concepts. Similar antennas that combine TA and RA are proposed in [12-17]. For these antennas, however, the bidirectional beams are not produced simultaneously, and their operation modes depend on polarization and frequency. Moreover, all the aforementioned examples use dielectric materials [11-17]. A design of metal-only TRA (MOTRA) is proposed in [18] that consists of Babinet-inverted defected square slot cells etched on a single-layer thin metallic sheet.

The present contribution is based on the original concept of three-dimensional (3D) MORA PC that was proposed in

[19-20] for RA designs. The main novelty here is that the short-circuit terminated the cell is removed. This modification allows the 3D PC to manipulate both reflected and transmitted waves. The cell consists of concentric square metal waveguides with open terminations. Thanks to its 3D configuration, it offers more flexibility and new possibilities compared to slot-type cells. As a validation, two MOTRAs are designed. Simulation results are presented in this paper. To the best knowledge of the authors, it is the first time a waveguide-based cell is used to design a TRA. Also, it is the first time the concept of PCs is introduced for TRAs.

Finally, the fabrication of such 3D waveguide-based structure is easy and cheap thanks to the development of 3D printing technology. As an experimental demonstration, a MOTRA made of PCs is fabricated using selective laser melting technology and measured. This is the second contribution of this paper.

The paper is organized as follows. Part II provides a detailed analysis of the proposed PC. Part III describes the design and the simulation of two different TRAs operating at 16 GHz. Then, in part IV, a MOTRA is fabricated and measured to further validate the proposed PC. Finally, a conclusion is drawn in part V.

II. UNIT CELL ANALYSIS

The waveguide-based PC, as shown in Fig.1, consists of two concentric square metallic waveguides and a square metallic block at the center. The external dimension (L_c) is set to 9.375 mm ($\lambda_0/2$ at the central frequency, 16 GHz) to prevent from grating lobes in an array configuration.

The presence of the inner square waveguide decreases the cut-off frequency of the fundamental TE_{10} and TE_{01}-like modes in the outer waveguide so that they can propagate at the operating frequency [20]. Its size (L_r) is varied to control the cell behavior. Before analyzing the principle of this PC, the characteristics of the two waveguides are simulated first (see Fig.2). It can be seen from Fig.2a and b that the inner waveguide always operates below cutoff at 16GHz while the outer waveguide almost always operates in the propagative mode. Note that a medium value (1.5mm) of the size of the central metallic block is chosen so that the behavior of the PC is mainly controlled by the outer waveguide and also to minimize weight.

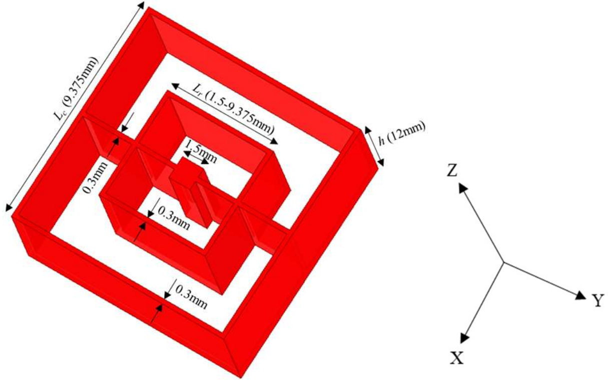

a)

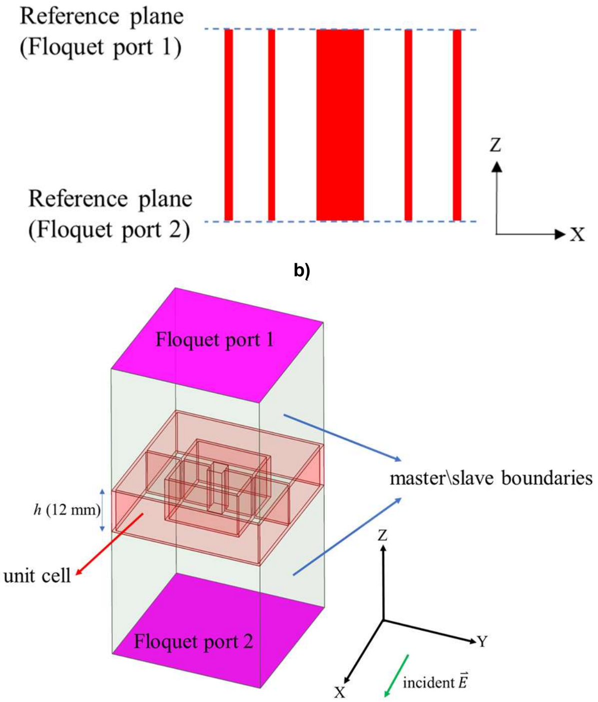

b)

c)

Figure 1. The proposed unit cell. a) 3D view. b) Sectional view. c) Simulation setup.

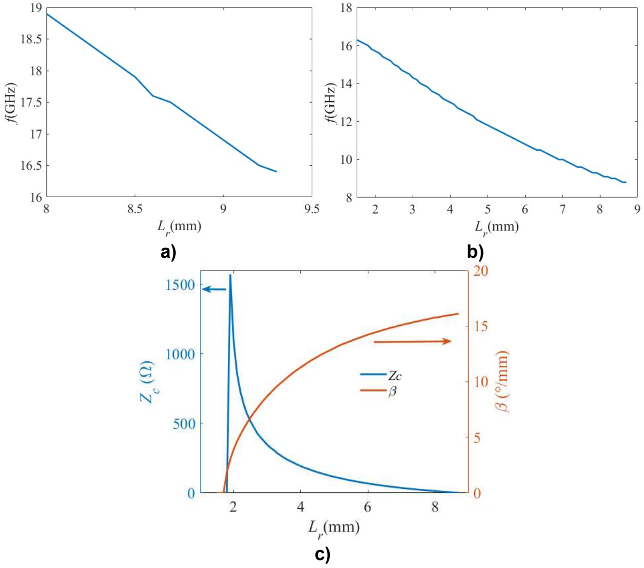

a)

b)

c)

Figure 2. The characteristics of the two waveguides. a) Cutoff frequency of inner waveguide. b) Cutoff frequency of outer waveguide. c) Characteristic impedance (*Zc*) and propagation constant (*β*) of outer waveguide.

When an incident electromagnetic wave impinges on port 1, both transmitted and reflected waves are produced. Reflection is due to the initial reflection at port 1 but also to multiple reflections between ports 1 and 2. It is then dependent on h, β and Zc where the latter two terms are defined in Fig. 2c and are mainly affected by the cross section of the waveguide (L_r). Reflection produces radiation in the backward direction (half space above port 1). Now, the transmitted wave is radiated at port 2 in the forward direction

This article has been accepted for publication in IEEE Access. This is the author's version which has not been fully edited and
content may change prior to final publication. Citation information: DOI 10.1109/ACCESS.2023.3338150

(half space beyond port 2). It is mainly controlled by the propagation through the outer waveguide. If the length of the cell is not long enough, some power can also couple directly from port 1 to port 2 through the inner waveguide.

The PC is simulated using HFSS@ to better illustrate its operation principle. The simulation setup is shown in Fig.1 c). It is illuminated under normal incidence with a x-polarized wave. Floquet ports are used and master slave boundary conditions are assigned on the lateral faces of the cell to mimic a periodic infinite environment. The height (h) is set to 12 mm (as will be justified later on) and metal parts are represented by Perfect Electric Conductor (PEC). Fig.3 shows the simulated magnitude in dB of the S-parameters at 16 GHz when L_r is varied. For values of L_r lower than 2.3 mm, the magnitude of S_{21} is quite small. This is explained by the high characteristic impedance or the cutoff mode of the outer waveguide, as shown in Fig.2c. Since most of the incident wave is reflected back, the cell can operate as a RA cell. With the increase of L_r, the characteristic impedance of outer waveguide decreases and approaches that of free space, Z_0 (see Fig.2c). Thus, the incident wave is now coupled to the outer waveguide. In this case, $|S_{21}|$ gets close to 1 and the PC can operate as a TA cell. For L_r larger than 6.8 mm, the characteristic impedance of outer waveguide decreases further (see Fig.2c), the waveguide is mismatched, and the PC can operate as a RA cell again. These results suggest that a TRA could be designed, where some cells are used to control the reflected beam and the other ones are used to control the transmitted beam.

In order to have a more global view, both h and L_r are now varied. The simulated S-parameters of the PC at 16 GHz are shown in Fig.4. On the one hand, it appears that the region where the cell can best be used for reflection is when $5<L_r<9$ mm with $h<10$ mm (left bottom region of Fig. 4c, where $|S_{11}|$ is close to 1). In this region, the characteristic impedance of the outer waveguide is far from Z_0 (see Fig.2c) and most of the incident wave is reflected back directly at the input port. Unfortunately, a direct consequence of this mechanism is that the range of achievable reflected phases (Fig. 4a) is quite reduced since the incident wave does not penetrate into the cell. On the other hand, the appropriate region for transmission is either when $L_r<5$ mm or, best, when $h>10.6$ mm. The latter case not only provides a magnitude of $|S_{21}|$ close to 1 but also a full 360° range for the transmitted phase (Fig. 4b).

Fig. 4c and 4d also exhibit regions with very low reflection or transmission (dark blue lines). They are associated with phase jumps, as can be seen in Fig. 4a and 4b. In order to have a deeper insight into these resonant phenomena, multiple reflections have to be considered. Assuming the wave only propagates inside the outer waveguide, theoretical approximations of the S-parameters are given by:

$$S_{21}^{th} = \frac{(1-\Gamma^2)e^{-j\beta h}}{1-\Gamma^2 e^{-2j\beta h}} \qquad (1)$$

$$S_{11}^{th} = \frac{\Gamma\left(1-e^{-2j\beta h}\right)}{1-\Gamma^2 e^{-2j\beta h}} \qquad (2)$$

where Γ expresses the mismatch between the external waveguide and free space:

$$\Gamma = \frac{Z_c - Z_0}{Z_c + Z_0} \qquad (3)$$

Note that (3) is only an approximation as discontinuity effects also arise at the input and output ports [20].

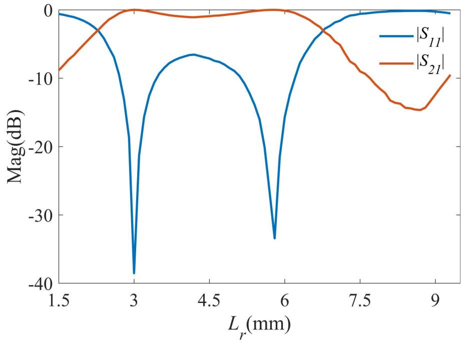

Figure 3. Magnitude of S-parameters of the PC (*h*=12 mm, *f*=16 GHz, x-polarization, normal incidence).

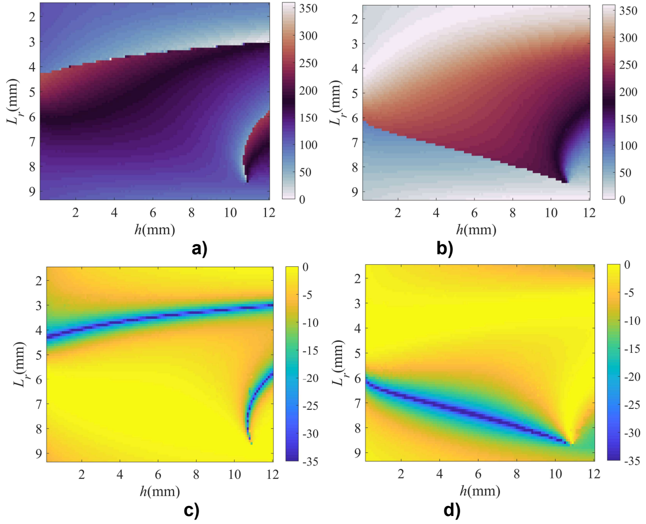

a)
b)
c)
d)

Figure 4. Simulated S-parameters at 16 GHz, x-polarization, normal incidence. a) Phase (S_{11}) (deg). b) Phase (S_{21}) (deg). c) Mag (S_{11}) (dB). d) Mag (S_{21}) (dB).

Fig.5 plots the theoretical S-parameters where the variations of both Z_c and β versus L_r are taken into account (using full-wave simulations of the outer waveguide). The agreement with Fig. 4 (full-wave simulations of the whole cell itself) is quite good, in spite of the approximations in the theoretical model. This suggests equations (1) and (2) provides a comprehensive means to analyze the cell, at least qualitatively. The two dark blue lines in Fig. 4c are first considered. In this particular case, the agreement with Fig.5c is good. The top curve in Fig.5c is obtained for L_r equal to 2.9 mm. It can be seen from Fig. 2c that this value corresponds to the case where the characteristic impedance of the outer waveguide is exactly equal to Z_0, leading to a perfect matching and a total transmission. Now, the bottom curve in Fig.5c involves L_r values ranging from 6.3 mm to 8.7 mm and h values ranging from 11.2 mm to 12 mm. For such values of L_r, the characteristic impedance of the outer waveguide varies from 1.24 Ω to 57.62 Ω, which

This article has been accepted for publication in IEEE Access. This is the author's version which has not been fully edited and
content may change prior to final publication. Citation information: DOI 10.1109/ACCESS.2023.3338150

corresponds to a quite large magnitude of Γ. Then, a Fabry-Perot resonance occurs as soon as βh is equal to π. As a result, $|S_{21}|$ gets close to 1, meaning $|S_{11}|$ is minimal.

Now, the dark blue line in Fig.4d is analyzed, which corresponds to a minimum of transmission. Its equivalent in Fig. 5d is not a straight line but still a region of low transmission. Once again, the imperfect agreement is due to the used approximations in the theoretical model. Indeed, in this case, the value of L_r is close to that of L_c, which means the cut-off frequency of the inner waveguide is not far from the operating frequency and its effect is not negligible any longer. However, equation (3) suggests this low-transmission region is associated to a value of Γ such that $\Gamma^2\approx1$, which is consistent with the low values of Z_C in this range of L_r.

Finally, it is worth pointing out that the interesting region for transmission (h>10.6 mm) is quite well predicted in Fig. 5d. As already mentioned, it is related to the Fabry-Perot resonance (bottom dark blue curve in Fig. 5c), which highlights the importance of this phenomenon in the achievement of a full 360° range for transmitted phase.

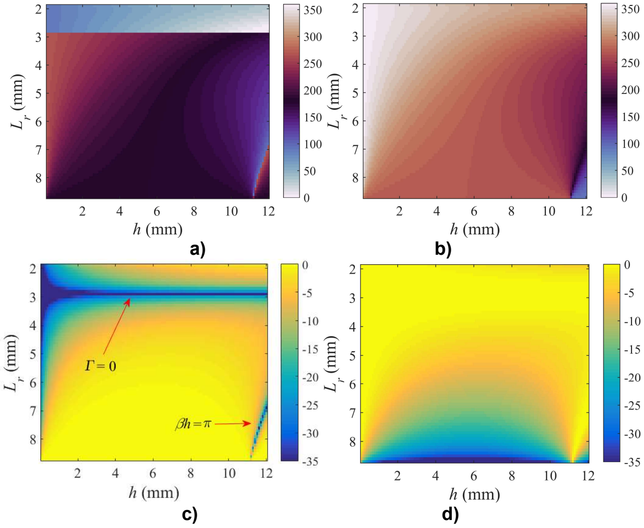

Figure 5. Theoretical S-parameters at 16 GHz with x-polarized incident wave under normal incidence. a) Phase (S_{11}^{th}) (deg). b) Phase (S_{21}^{th}) (deg). c) Mag (S_{11}^{th}) (dB). d) Mag (S_{21}^{th}) (dB).

III. ANTENNA DESIGN

In this section, two different TRAs are designed to validate the capability of the proposed PC. Both TRAs produce a reflected beam at 15° from broadside but they differ by the direction of the transmitted beam. As summarized in TABLE I, TRA1 produces a transmitted beam that is symmetrical to the reflected one while TRA2 steers the transmitted beam in a different plane (also see Fig.9d and Fig.10e and f). Note that the angles in table I indicate the directions of both transmitted and reflected beams produced by two TRAs and they are based on the angle of (theta, phi).

The two TRAs use the same configuration. The center frequency is 16GHz. The illumination is achieved by a linearly polarized horn antenna with an offset angle of 15° with respect to the normal of the panel. The radiating aperture is 13λ₀× 13λ₀ (λ₀ is the wavelength at the center frequency). The f/d ratio is 1.1.

The synthesis process consists in selecting the geometry for each cell in the TRA in order to achieve best the desired phase. The desired phase law at frequency f is defined by:

$$\phi_m^{des}(f) = \frac{2\pi f}{c}\left[R_m - \begin{pmatrix} x_m \sin\theta_0 \cos\varphi_0 + \\ y_m \sin\theta_0 \sin\varphi_0 \end{pmatrix}\right] + \phi^{off}(f) \qquad (4)$$

where R_m is the distance between the feed phase-center and cell m in the RA, (x_m, y_m) are the coordinates of this cell, (θ_0, φ_0) the direction of the main beam and c is the speed of light. ϕ^{off} is a phase offset that is optimized during the synthesis process to minimize the total phase error ε, defined as:

$$\varepsilon = \sum_{m=1}^{N_c} I_m \begin{bmatrix} |S_{11}^m||\phi_{R,m}^{ac} - \phi_{R,m}^{des}| \\ +|S_{21}^m||\phi_{T,m}^{ach} - \phi_{T,m}^{des}| \end{bmatrix} \qquad (5)$$

where index R and T refer to the TA and RA phases respectively while S_{11}^m and S_{21}^m are the scattering parameters of cell m. N_c is the total number of the cells in the array. I_m is the illumination intensity of each cell in the array. It corresponds to the complex magnitude of the incident field at the top surface of each cell. Note that, for the sake of simplicity, the optimization is done here for the central frequency only (16 GHz).

The synthesis process can be summarized as follows:

1) The phase offsets in (4) are first set to 1° for both the reflected and transmitted beams.

2) For given phase offsets, the geometry of each cell is selected in order to minimize its contribution to the weighted phase error in equation (5). In this step, the phase achieved by a given geometry is calculated using the database in Fig. 6 that accounts for oblique incidence (at the center of the array).

3) The phase offsets are increased progressively up to 360° with a step of 1°, so that all possible combinations of offsets are considered. Each time one of the offsets is updated, step 2 is repeated.

4) The combination of offsets that produces the minimum total phase error is selected and the corresponding cell geometries are used to synthesize the TRA.

As already observed in Fig.4, a large h is needed to provide a 360° range for the transmission phase. This is why h is set to 12 mm. Also, the incident wave is x-polarized to comply with the additional constraint brought by the lateral metallic wall at the middle of the cells.

The simulated database at 16 GHz is given in Fig.6. It shows certain cells (typically those with $|S_{11}|$>-2 dB) seem best suited for reflection and other ones ($|S_{21}|$>-2 dB) for transmission. The remaining ones are neither optimal for reflection nor transmission.

Note that the cells in the transition zone (see Fig.6) are not removed from the database because they also contribute to the transmitted and reflected beams. In the end, it must be highlighted that it is the optimization process itself that decides whether a cell is used for TA or RA and this is done automatically by minimizing the weighted phase error as given by (5). In other words, the number of the TA and RA cells is balanced by the optimization process itself.

TABLE I
DETAILED PARAMTERS OF TWO TRAS

	Direction of transmitted beam	*Direction of reflected beam*
TRA1	(165°, 270°)	(15°, 270°)
TRA2	(155°, 0°)	(15°, 270°)

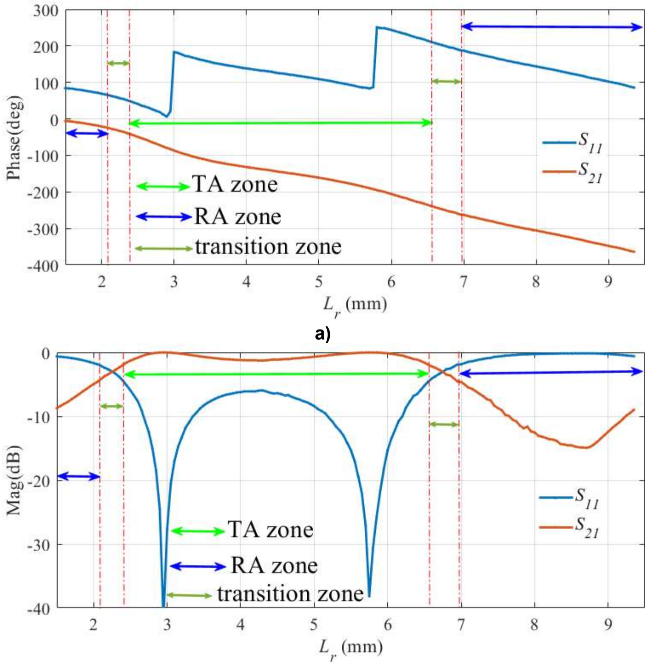

a)

b)

Figure 6. The simulated S-parameters (*h*=12 mm, step=0.05 mm, *f*=16 GHz, x-polarization, ϕ_{inc}=90°, θ_{inc}=15°). a) Phase. b) Magnitude.

As a final figure of merit, the average achieved phase error is defined as:

$$\bar{\varepsilon} = \sum_{m=1}^{N_c} I_m \left[\frac{|S_{11}^m|\left|\phi_{R,m}^{ach}-\phi_{R,m}^{des}\right|}{\sum_{m=1}^{Nc} I_m|S_{11}^m|} + \frac{|S_{21}^m|}{\sum_{m=1}^{Nc} I_m|S_{21}^m|}\left|\phi_{T,m}^{ach}-\phi_{T,m}^{des}\right| \right] \quad (6)$$

The achieved average phase errors of both TRAs are 8.77° and 43.20° respectively. Note that, if the directions of both reflected and transmitted beams are symmetrical (TRA1), the required phases for reflection and transmission are identical. In this case, it is quite easy to select offset phases for reflection (ϕ_R^{off}) and transmission (ϕ_T^{off}) so that each cell almost meets the required phases for both beams simultaneously. Therefore, the total phase error in (5) can easily be minimized. As a result, a much lower phase error is obtained for TRA1.

The distributions of TA cells and RA cells in the two TRAs are shown in Fig.7. The green color, the blue color and the dark green color in Fig.7 represent the RA cells, the TA cells and the transition cells respectively. In addition, TABLE II compares the two TRAs.

To limit fabrication issues, cells where the gap between two metal walls is less than 0.2 mm are not accepted in the final design. Consequently, these gaps are suppressed (filled with metal).

TABLE II
COMPARISON BETWEEN BOTH TRAS

		AvgError $\sum_{m=1}^{N_c}\frac{I_m\|S_{11}^m\|\|\phi_{R,m}^{ach}-\phi_{R,m}^{des}\|}{\sum_{m=1}^{N_c} I_m\|S_{11}^m\|}$ or $\sum_{m=1}^{N_c}\frac{I_m\|S_{21}^m\|\|\phi_{T,m}^{ach}-\phi_{T,m}^{des}\|}{\sum_{m=1}^{N_c} I_m\|S_{21}^m\|}$	**Number of cells**	**Total weighting coefficient** $\sum_{m=1}^{N_c} I_m\|S_{21}^m\|$ or $\sum_{m=1}^{N_c} I_m\|S_{11}^m\|$
TRA1	TA	7.79°	346	0.6733
	RA	0.99°	296	0.5533
TRA2	TA	25.34°	447	0.7492
	RA	17.86°	210	0.4271

Fig.8 shows TRAs with the associated radiated field at 16 GHz, showing that both transmitted and reflected beams are produced simultaneously. The performance of TRA1 is analyzed first. The achieved gain for transmission and reflection is 27.2dBi and 27.1dBi respectively. The corresponding aperture efficiency is 24.71% and 24.15% respectively. The total aperture efficiency of TRA1 is defined from the sum of both reflected and transmitted powers. Therefore, the achieved aperture efficiency for TRA1 is 48.86%. The reflected beam and the transmitted beam of TRA1 achieve similar performances, which is consistent with the quite similar characteristics obtained in Table II regarding the cell numbers and weighting coefficients for both configurations. The normalized radiation patterns at 16 GHz are shown in Fig.9, Z' and Z'' indicate the directions of reflected beam and transmitted beam respectively. The beams in such figure are produced in the desired directions, which demonstrates the ability of the proposed PC to design TRAs. Also, the side lobe and the cross polarization are lower than -15.3 dB and -36.0 dB, respectively.

For TRA2, the achieved gain in transmission and reflection at 16 GHz is 26.0 dBi and 22.4 dBi, respectively. The corresponding aperture efficiency is 18.75% and 8.15%, respectively. Obviously, the performance for transmission is better than that for reflection, which is consistent with the double number of cells used for transmission. In addition, the achieved total aperture efficiency of TRA2 is reduced compared to TRA1, which is due to the significant increase in average phase error (see TABLE. II). The normalized radiation patterns at 16GHz are shown in Fig.10. The side lobe and the cross polarization are lower than -10.7dB and -28.8dB respectively.

This article has been accepted for publication in IEEE Access. This is the author's version which has not been fully edited and content may change prior to final publication. Citation information: DOI 10.1109/ACCESS.2023.3338150

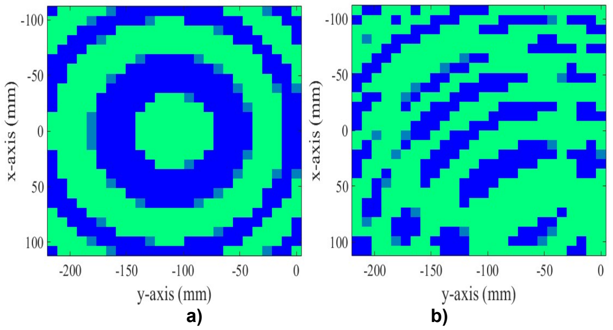

Figure 7. The distribution of TA cells (green), RA cells (blue) and transition cells (dark green). a) TRA1. b) TRA2.

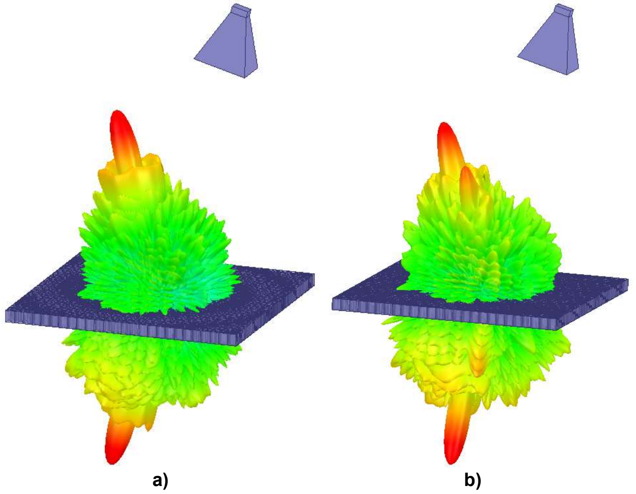

Figure 8. TRAs and horn with associated beams at 16GHz. a) TRA1. B) TRA2.

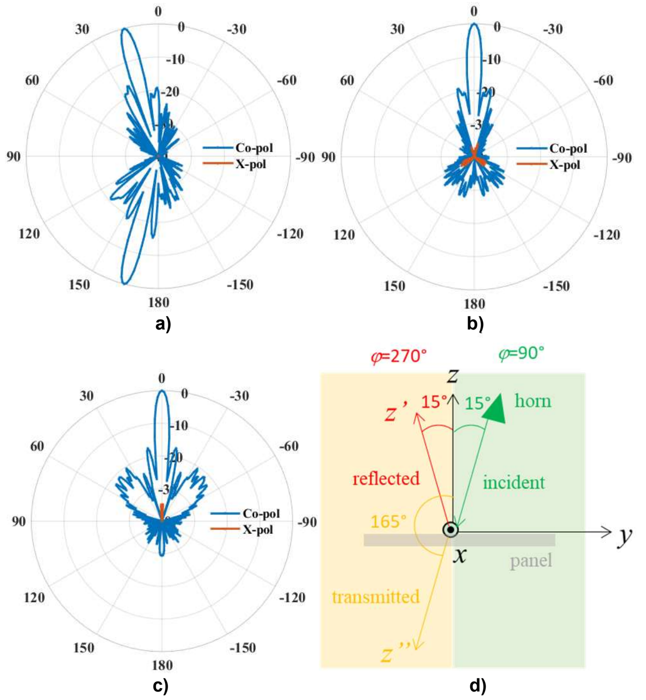

Figure 9. Normalized radiation patterns of TRA1 (dB) at 16 GHZ. a) yoz plane. b) xoz' plane. c) xoz'' plane. d) antenna configuration

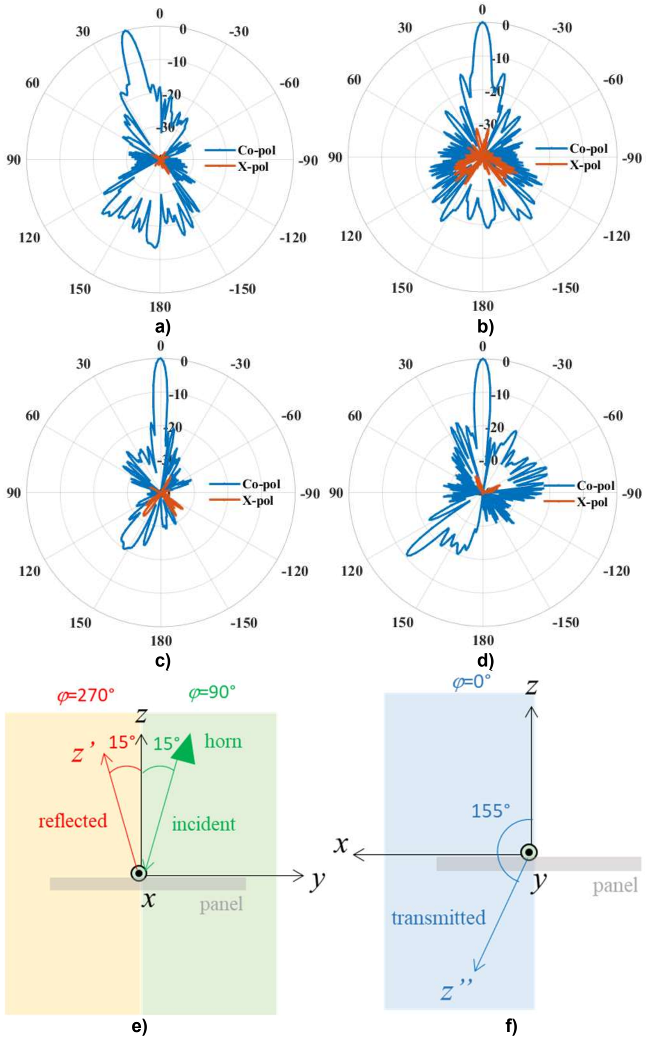

Figure 10. Normalized radiation patterns of TRA2 (dB) at 16 GHz - a) yoz plane (reflected beam). b) xoz' plane (reflected beam). c) yoz'' plane (transmitted beam). d) xoz'' plane (transmitted beam). e) antenna configuration (reflected beam). f) antenna configuration (transmitted beam).

IV. FABRICATION AND MEASUREMENTS

TRA1 is fabricated and measured to further demonstrate the capabilities of the proposed PC. The TRA and horn antenna are fabricated layer by layer using selective laser melting 3D printing technology. During the fabrication, the antenna is under nitrogen atmosphere at 100W/240W (border/volume) laser power (λ=1075 nm). The material used is a 316L stainless steel powder with a diameter distribution between 10 and 45 μm. Note that the wall thickness (see Fig.1a) is set to 0.3mm, which was found to be the minimal achievable value in order to comply both with robustness and accuracy. Fig.11 shows the photographs of manufactured TRA and measurement setup.

The antenna is measured in the anechoic environment of the near-field compact-range multi-probe Over-The-Air testing system MVG / Satimo StarLab (see Fig.11b). The comparison of simulated and measured radiation patterns (from 15 to 18GHz) is shown in Fig.12. It can be observed

This article has been accepted for publication in IEEE Access. This is the author's version which has not been fully edited and content may change prior to final publication. Citation information: DOI 10.1109/ACCESS.2023.3338150

from Fig.12 that a good agreement between simulation and measurement is achieved. The difference between the direction of the simulated and measured main beams can be attributed to an inappropriate phase center, which is caused by the deformation of the plastic arm supporting the feed horn (see Fig.11b). To minimize the difference, additional foam is added to support the arm (see Fig.11b).

It can also be seen from Fig.12 that the measured side lobe level and cross polarization level are -14.7/-15.3/-13.4/-12.2 dB and -24.5/-23.1/-31.9/-25.2 dB at 15/16/17/18 GHz. These results are completely acceptable.

The gain response from 15 to 18GHz is shown in Fig.13. It can be seen that the maximum gain difference between simulation and measurement is less than 3.7dB. First, the inappropriate phase center can directly increase the phase error of all cells in the array, leading to a decrease in gain. Furthermore, errors in fabrication process can also degrade the gain. It can also be seen from Fig.13 that the measured 1-dB gain bandwidth of reflected beam is 6.25% (from 15.5 to 16.5GHz) while that of transmitted one is 11.11% (from 16 to 18GHz). In addition, the measured gain and aperture efficiency for transmitted (reflected) beam at 16GHz are 25.7 dB (24.1 dB) and 17.49% (12.39%) respectively. As a summary, the results in Fig.12 and 13 demonstrate that the fabricated antenna can achieve the TRA's functionalities.

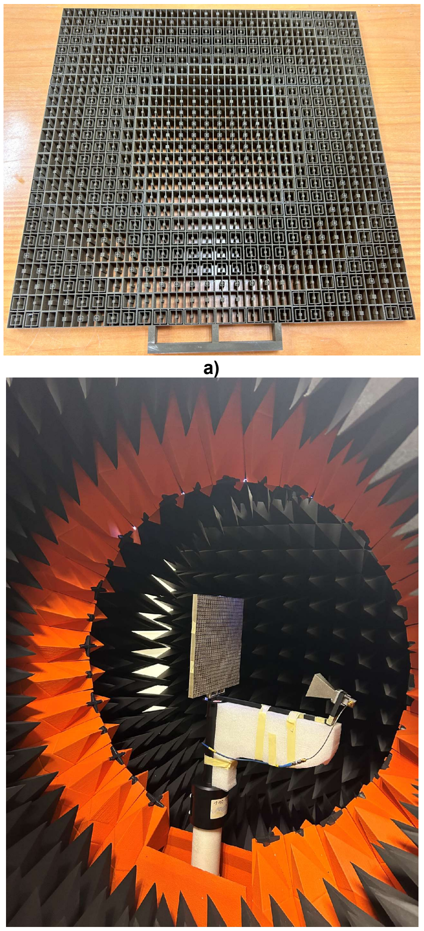
a)

b)

Figure 11. Photographs of: a) manufactured TRA. b) measurement setup.

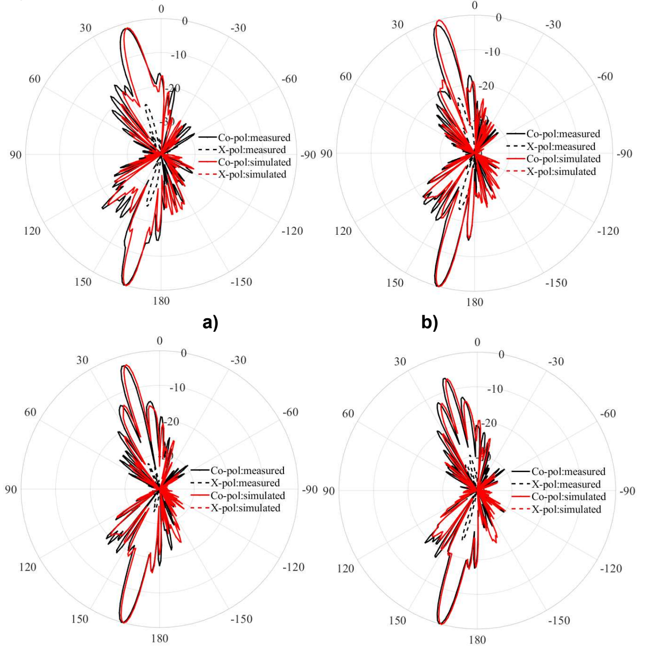

a)
b)
c)
d)

Figure 12. Comparison of simulated and measured radiation patterns (yoz plane). a) 15GHz. b) 16GHz. c) 17GHz. d) 18GHz.

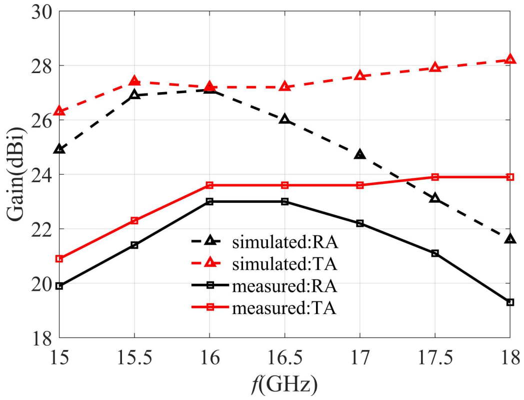

Figure 13. Comparison of simulated and measured gain.

V. BENCHMARKETING

The proposed cell in this article is a modification of the original PC presented in [20] for a pure RA application. For such a RA configuration, the PC consists of two concentric waveguides with a short-circuit termination which is used to completely reflect the incident wave. As here, the size of the inner waveguide is used to control the reflection phase. However, there are two main differences between the original PC in [20] and the one in this article. Firstly, the short-circuit termination that is used in [20] at port 2 (see Fig.1a) is replaced here by an open-ended one in order to let the transmitted wave within the waveguide be radiated beyond port 2. Secondly, since the short-circuit termination has been removed, no more ground plane is available here to hold all metallic parts together. This is why a transverse metallic wall is added at the middle of the cell in the *y* direction (see Fig. 1a again), acting as a support. Therefore, contrarily to the original PC in [20] that is dual-polarized, the present one only enables *x*-polarization. As a summary, the original PC in [20] can only be used for a RA configuration while the present PC enables to generate both reflected and transmitted beams simultaneously.

One interesting prospective would be to use this new cell for dual-polarization. Indeed, the added transverse metal wall produces full reflection for an impinging *y*-polarized incident wave. By properly optimizing its dimensions, it should be possible to produce an additional reflected beam in a different direction for *y*-polarization.

VI. CONCLUSION

In this work, a 3D MO PC is proposed. It uses open-ended waveguides to control the reflection and transmission phases. A complete analysis of the cell is provided by considering multiple reflections to explain its operation principle. Two MOTRAs made of PCs are designed. Simulation results show that they have the ability to produce both transmitted and reflected beams simultaneously. When the directions of the two beams are symmetrical, the characteristics of both beams are similar, and the performance is better. The TRA with symmetrical beams is fabricated using selective laser melting technology to further validate the proposed 3D MO PC. Measurement results show that a good agreement between the simulated and measured radiation patterns is achieved. The measured 1-dB gain bandwidth for reflected and transmitted beams are 6.25% and 11.11% respectively. Both the simulation and measurement results of TRAs demonstrated the proposed 3D MO PC.

ACKNOWLEDGMENT

The authors would like to thank Jérôme Sol for measurements.

REFERENCES

[1] L. Moustafa, R. Gillard, F. Peris, R. Loison, H. Legay, and E. Girard, “The Phoenix Cell: A New Reflectarray Cell With Large Bandwidth and Rebirth Capabilities,” Antennas Wirel. Propag. Lett., vol. 10, pp. 71–74, 2011.

[2] R. Deng, S. Xu, F. Yang, and M. Li, “Single-Layer Dual-Band Reflectarray Antennas With Wide Frequency Ratios and High Aperture Efficiencies Using Phoenix Elements,” IEEE Trans. Antennas Propagat., vol. 65, no. 2, pp. 612–622, Feb. 2017.

[3] X. Li, X. Li, and L. Yang, “Single-Layer Dual-Band Wide Band-Ratio Reflectarray With Orthogonal Linear Polarization,” IEEE Access, vol. 8, pp. 93586–93593, 2020.

[4] A. Bornot, B. Palacin, M. Romier, L. Feat, and D. Belot, “A Single-Layer Reflectarray Using Hexagonal Phoenix Cells for Ka-band Applications,” in 2021 15th European Conference on Antennas and Propagation (EuCAP), Dusseldorf, Germany: IEEE, Mar. 2021, pp. 1–5.

[5] V. Richard et al., “Spherical Mapping of the Second-order Pheonix Cell for Unbounded Direct Reflectarray Copolar Optimization,” PIER C, vol. 90, pp. 109–124, 2019.

[6] H. Salti and R. Gillard, “A Statistical Approach for Gain Bandwidth Prediction of Phoenix-Cell Based Reflect arrays,” Adv. sci. technol. eng. syst. j., vol. 3, no. 1, pp. 103–108, Jan. 2018.

[7] T. Makdissy et al., “Phoenix’ reflectarray unit cell with reduced size and inductive loading,” IET Microw. Antennas Propag., vol. 10, no. 12, pp. 1363–1370, Sep. 2016.

[8] A. Guarriello, G. Courtin, R. Loison, and R. Gillard, “A General Equivalent Circuit Model for Phoenix Cells,” IEEE Trans. Antennas Propagat., vol. 69, no. 11, pp. 7982–7986, Nov. 2021.

[9] J. Coonrod and J. Davis, “Sending Circuit Materials Into Space,” Microwave Journal.

[10] A. H. Abdelrahman, F. Yang, A. Z. Elsherbeni, and P. Nayeri, Analysis and Design of Transmitarray Antennas. San Rafael, CA, USA: Morgan & Claypool, 2017

[11] S. L. Liu, X. Q. Lin, Y. H. Yan, and Y. L. Fan, “Generation of a High-Gain Bidirectional Transmit–Reflect-Array Antenna With Asymmetric Beams Using Sparse-Array Method,” IEEE Trans. Antennas Propagat., vol. 69, no. 9, pp. 6087–6092, Sep. 2021.

[12] X. Liu, Z. Yan, E. Wang, X. Zhao, T. Zhang, and F. Fan, “Dual-Band Orthogonally-Polarized Dual-Beam Reflect-Transmit-Array With a Linearly Polarized Feeder,” IEEE Trans. Antennas Propagat., vol. 70, no. 9, pp. 8596–8601, Sep. 2022.

[13] X. Li et al., “Dual-Band Wideband Reflect-Transmit-Array With Different Polarizations Using Three-Layer Elements,” Antennas Wirel. Propag. Lett., vol. 20, no. 7, pp. 1317–1321, Jul. 2021.

[14] W. Yang, K. Chen, and Y. Feng, “Multifunctional Metasurface for Broadband Reflect-Transmit-Array Antenna at 5G Millimeter-Wave Band,” in 2022 16th European Conference on Antennas and Propagation (EuCAP), Madrid, Spain: IEEE, Mar. 2022, pp. 1–5.

[15] J. Feng et al., “Reflect–Transmit-Array Antenna With Independent Dual Circularly Polarized Beam Control,” Antennas Wirel. Propag. Lett., vol. 22, no. 1, pp. 89–93, Jan. 2023.

[16] W. Song et al., “A Single-Layer Reflect-Transmit-Array Antenna With Polarization-Dependent Operation,” IEEE Access, vol. 9, pp. 167928–167935, 2021.

[17] S. Liu and Q. Chen, “A Wideband, Multifunctional Reflect-Transmit-Array Antenna With Polarization-Dependent Operation,” IEEE Trans. Antennas Propagat., vol. 69, no. 3, pp. 1383–1392, Mar. 2021.

[18] F. Yang, R. Deng, S. Xu, and M. Li, “Design and Experiment of a Near-Zero-Thickness High-Gain Transmit-Reflect-Array Antenna Using Anisotropic Metasurface,” IEEE Trans. Antennas Propagat., vol. 66, no. 6, pp. 2853–2861, Jun. 2018.

[19] T. Makdissy, R. Gillard, Z. An, and S. Vaudreuil, “Dual linearly polarised 3D printed phoenix cell for wide band metal only reflectarrays,” IET Microw. Antennas Propag., vol. 14, no. 12, pp. 1411–1416, Oct. 2020

[20] Z. An, T. Makdissy, M. G. Vigueras, S. Vaudreuil, and R. Gillard, “A Metal-Only Reflectarray Made of 3D Phoenix Cells,” in 2022 16th European Conference on Antennas and Propagation (EuCAP), Madrid, Spain: IEEE, Mar. 2022, pp. 1–5.

ZHIHANG AN received the B.S. degree from China University of Geosciences (Beijing) in 2016, the M.S. degree from Beijing Jiaotong University in 2019 and the Ph.D. degree in electronics from the Institut d’Électronique et des Technologies du numéRique (IETR), Rennes, France in 2023.

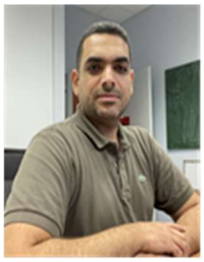

TONY MAKDISSY was born in Lebanon in 1986. In 2010 he received both the Engineering degree and the Master of Research degree in Electronics & Telecommunication, respectively from the Lebanese University and from the National Institute of Applied Sciences (INSA), Rennes-France. In 2013, he received the PhD degree from INSA, then signed a one-year contract as an Instructor-Researcher in the department of Communication Systems and Networks.

From January 2015 to August 2016, he joined several Universities and Engineering Schools in Lebanon as a part-time lecturer. In September 2016, he joined the Faculty of Engineering at the Université Antonine (UA),

This article has been accepted for publication in IEEE Access. This is the author's version which has not been fully edited and content may change prior to final publication. Citation information: DOI 10.1109/ACCESS.2023.3338150

Baabda-Lebanon, as a full-time faculty member. During his four years at the UA, Dr Makdissy held several responsibilities. Among others, he was elected as the representative of the full-time instructors in UA's board for 2018/2019, and he was appointed the Assistant Dean position at the Faculty of Engineering from 2019 to 2020. In 2018, he won the UA's annual scientific research award as the best researcher of the year. In November 2020, he joined the Institut Jean Lamour, Nancy-France as a Research Fellow. Since March 2022, he is with SOITEC as a R&D engineer in the business unit Filters. His main research interests are passive and reconfigurable reflectarrays, antenna packaging solutions for surface acoustic wave (SAW) sensors, mmWave filters, and characterization of piezoelectric-on-insulator stacks for SAW filters.

MARÍA GARCÍA-VIGUERAS (Member, IEEE) was born in Murcia, Spain. She received the M.Sc. degree in telecommunications engineering and the Ph.D. degree from the Technical University of Cartagena, Cartagena, Spain, in 2007 and 2012, respectively.

From 2012 to 2015, she was a Research Fellow with the Laboratory of Electromagnetism and Antennas, École Polytechnique Fédérale de Lausanne, Lausanne, Switzerland. She is currently an Associate Professor with the Institute National des Sciences Apliquées de Rennes, INSA Rennes, France. She has coauthored more than 30 IEEE journals and 50 publications in international conferences. Her current research interests include leaky wave antennas, periodic surfaces, active antennas, waveguide feed chain components, and the evaluation of additive manufacturing’s potential for RF design.

Dr. García-Vigueras is a junior member of the Institute Universitaire de France (IUF) during the period 2023-2028, with the Innovation Chair. From 2021, she is the co-chair of the EurAAP working group Women in Antennas and Propagation (WiAP). She has been the recipient of several prizes, including two Best Ph.D. Thesis Awards from COIT/AEIT in 2014 and UPTC in 2013, respectively (in Spain), the Best Paper Awards in MAPE 2013 in Chengdu (China) and EuCAP 2012 in Prague (Czech Republic), and the EuMA Roberto Sorrentino prize in 2023 in the European Microwave Week of Berlin (Germany).

SÉBASTIEN VAUDREUIL was born in Quebec City, QC, Canada in 1973. He received the Ph.D. degree in Chemical Engineering from the Université Laval (Quebec City) in 2003.

From 2002 to 2005, he was a Research Engineer at the Arvida Research & Development Center of Alcan Inc. (now part of Rio Tinto). In Morocco since 2008, he occupied successively the position of Director of the Technological Platform at MAScIR between 2008 and 2011, and of Full Professor at the Euromed University of Fez since 2013. He is the author of more than 80 papers. His research interests include Additive Manufacturing, Renewable Energies, Energy Storage, and Water Desalinization. He is currently a registered engineer at Ordre des Ingénieurs du Québec (OIQ).

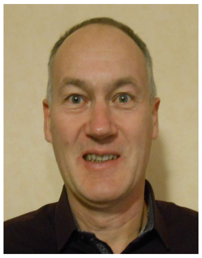

RAPHAËL GILLARD was born in Ernée, France, in 1966. He received the PhD degree in Electronics from INSA Rennes, France, in 1992.

He first worked as a research engineer in IPSIS company, Cesson-Sévigné, France. He joined INSA in 1993 as an assistant Professor and contributed to the development of EM solvers for antenna and circuits modelling. Since 2001, he has been a full Professor in the Antenna and Microwaves Group of the Institut d’Électronique et des Technologies du numéRique (IETR), Rennes, where he was first in charge of the EM Modelling and Optimization activity. From 2006 to 2020, he has been co-leading the Antenna and Microwaves Department of IETR. From 2015 to 2020, he has also been the academic responsible of the MERLIN lab, a joint laboratory between IETR and Thales Alenia Space. His main research interests are antenna arrays, reflectarrays and periodic structures. He has been teaching electromagnetics, microwaves and antennas and is responsible for a Master Program since 2020.